Asian Journal of Chemistry; Vol. 38, No. 11 (2026), 3089-3096
ASIAN JOURNAL OF CHEMISTRY
https://doi.org/10.14233/ajchem.2026.36880

Phyto-Mediated Fabrication of Zinc Oxide Nanoparticles *via Citrus medica* L. Extract: Physico-Chemical Characterization and Bio-Functional Properties

SAILAJA REDDI[1,2], KUDA ESWARA RAO[3,*], N. ANIL KUMAR[4], SWABHI SUNIL KUMAR[5], S. PRAMEELA DEVI[6], KELOTH BASAVAIAH[4] and BHARATH KUMAR NAIK KETHAVATH[2,*]

[1]Department of Chemistry, Government Degree College, Palakonda-532440, India
[2]Department of Chemistry, SKBR Government Degree College, Macherla, Guntur-522426, India
[3]Department of Chemistry, Visakha Institute of Engineering and Technology (VIET), Narava, Visakhapatnam-530027, India
[4]Department of Chemistry, AU College of Science and Technology, Andhra University, Visakhapatnam-530003, India
[5]Department of Engineering Chemistry, AU College of Engineering, Andhra University, Visakhapatnam-530003, India
[6]Department of Engineering Chemistry, SRKR Engineering College, Bhimavaram-534204, India

*Corresponding author: E-mail: kerchemi12@gmail.com

Received: 24 July 2026 *Accepted*: 26 October 2026 *Published online*: 13 November 2026 AJC-22540

An aqueous phyto-assisted co-precipitation approach was employed to synthesize zinc oxide nanoparticles (ZnO NPs) using *Citrus medica* L. leaf extract as a natural complexing and surface-stabilizing agent. The synthesized nanoparticles were examined by UV-Vis and FTIR spectroscopy, powder X-ray diffraction (XRD), field-emission scanning electron microscopy (FE-SEM), transmission electron microscopy (TEM) and BET surface area analysis. UV-Vis and FTIR analyses provided spectroscopic evidence of ZnO NPs formation, with an estimated optical bandgap of 3.32 eV. XRD analysis confirmed the hexagonal wurtzite crystal structure. FE-SEM and TEM images revealed predominantly quasi-spherical particles with an average diameter of 59 nm. BET analysis yielded a specific surface area of 35.231 m^2/g and a pore volume of 1.7268 cm^3/g. The antibacterial potential of the ZnO NPs was assessed against Gram-negative bacteria (*E. coli*, *V. cholerae* and *S. typhi*) and Gram-positive *S. aureus*, with concentration-dependent inhibitory activity observed across the tested strains. Their antioxidant potential was examined through DPPH radical scavenging, hydrogen peroxide scavenging and reducing power assays, which revealed concentration-dependent antioxidant responses.

Keywords: Plant mediated synthesis, Zinc oxide nanoparticles, Antibacterial activity, Antioxidant activity.

INTRODUCTION

Zinc oxide nanoparticles (ZnO NPs) have received considerable attention in materials science and biomedical research owing to their distinctive physical and chemical characteristics [1-3]. These include a direct bandgap of approximately 3.37 eV at 300 K, an exciton binding energy of 60 meV and good chemical stability [4]. Such properties make ZnO NPs suitable for applications in photocatalysis, solar cells, gas sensing and biomedical devices [5]. Several approaches, such as sol-gel processing, co-precipitation and hydrothermal synthesis, have been employed for their preparation [6]. These methods may require chemical additives, elevated temperatures and prolonged processing, raising concerns about energy consumption, chemical waste and the suitability of the resulting materials for biomedical applications.

Plant-mediated synthesis offers an alternative route in which naturally occurring phytochemicals participate in metal ion complexation, particle formation and surface stabilization. Microorganisms, fungi and plant extracts have been investigated as biological resources for nanoparticle synthesis [7-9]. Plant-based approaches are particularly attractive as they avoid the need for microbial culture maintenance and can be carried out through relatively simple aqueous procedures [10]. Various phytoconstituents, such as polyphenols, flavonoids and organic acids, can interact with metal precursor species and influence nucleation, crystal growth and particle aggregation [11]. Despite progress in plant-assisted ZnO NPs synthesis, the contribution of individual plant extracts to particle morphology, surface characteristics and crystallinity has not been sufficiently established. The relationship between extract composition and the resulting physico-chemical prop-

This is an open access journal, and articles are distributed under the terms of the Attribution 4.0 International (CC BY 4.0) License. This license lets others distribute, remix, tweak, and build upon your work, even commercially, as long as they credit the author for the original creation. You must give appropriate credit, provide a link to the license, and indicate if changes were made.

erties of ZnO NPs remains an important aspect of investigation [12].

Citrus medica L., commonly known as citron, belongs to the Rutaceae family and is recognized for its diverse phytochemical composition. Its leaves contain polyphenols, flavonoids, ascorbic acid and volatile constituents associated with antioxidant and antimicrobial properties [9,10]. Although the biological activities of *C. medica* L. extracts have received attention, their application in the synthesis of semiconductor nanomaterials has been explored to a lesser extent. The interactions between leaf-derived phytochemicals and zinc precursor ions may influence particle formation, surface characteristics and crystal growth. The extent to which these interactions affect the surface area, porosity and morphological features of ZnO NPs warrants further investigation [13,14].

In this study, ZnO NPs were synthesized through an aqueous phyto-assisted co-precipitation route using *C. medica* L. leaf extract as a natural complexing and surface-stabilizing agent [15,16]. The structural, optical and morphological characteristics of the synthesized material were examined using UV-Vis spectroscopy, UV-Vis diffuse reflectance spectroscopy (UV-DRS), FTIR, XRD, FE-SEM, TEM and BET surface area analysis. Its biological performance was examined through in vitro antibacterial assays against Gram-negative bacteria (*Escherichia coli*, *Vibrio cholerae* and *Salmonella typhi*) and Gram-positive bacteria (Staphylococcus aureus). Antioxidant activity was assessed using DPPH and hydrogen peroxide (H_2O_2) scavenging assays. The study examines the physicochemical characteristics of the plant-mediated ZnO NPs alongside their antibacterial and antioxidant properties.

EXPERIMENTAL

All chemical reagents used in this study were of analytical grade and were utilized without further purification. Zinc acetate dihydrate ($Zn(CH_3COO)_2{\cdot}2H_2O$), 2,2-diphenyl-1-picrylhydrazyl (DPPH), sodium hydroxide pellets, hydrogen peroxide and rose Bengal were procured from Merck, India. All solutions were prepared using Milli-Q water, which was also used throughout the synthesis and experimental procedures to ensure high purity and minimize contamination.

Preparation of *C. medica* L. leaf extract: Fresh leaves of *C. medica* L. were collected from the forest of Marrivalasa, India (18.1304º N, 82.7277º E) in October 2024. The plant was authenticated by Prof. S.B. Padal, Department of Botany, Andhra University, India and a voucher specimen (No. 23353) was deposited for future reference. The collected leaves were washed thoroughly with running tap water, followed by three rinses with Milli-Q water to remove surface impurities. They were shade-dried at room temperature (25-30 ºC) for 21 days and ground into a fine powder using a household blender. For aqueous extract preparation, 3 g of the powdered leaves was dispersed in 100 mL of Milli-Q water in a 250 mL Erlenmeyer flask and heated at 70 ºC for 45 min under continuous stirring to facilitate the extraction of water-soluble phytochemicals. The mixture was cooled to room temperature and filtered through Whatman No. 1 filter paper to remove the residual plant material. The resulting clear, yellowish-brown extract was collected in sealed bottles and stored at 4 ºC until further use in ZnO NP synthesis.

Green synthesis of ZnO NPs: ZnO NPs were prepared *via* a phyto-assisted co-precipitation method using *C. medica* L. leaf extract. In a standard synthesis process, 10 mLof 3% aqueous *C. medica* L. leaf extract solution was mixed with a 250 mL Erlenmeyer flask. Then, 1 M $Zn(CH_3COO)_2{\cdot}2H_2O$ solution (10 mL) was added, together with 10 mL of a 1 M NaOH solution. Appropriate dilution and reaction conditions were maintained by making up the volume to 100 mL with Milli-Q water. The total reaction mixture was further stirred on a hot plate at 70 ºC for 60 min over water bath. This was confirmed by the gradual appearance of a white precipitate in the solution mixture, which denotes the nucleation and growth of ZnO NPs.

Phytochemical constituents present in the leaf extract interact with zinc species through coordination and may adsorb onto the growing crystallite surfaces, which influence the particle formation and surface stabilization. At the end of the reaction, the mixture was cooled to room temperature, and the ZnO NPs were recovered from the supernatant by centrifugation at 8,000 rpm for 15 min. The supernatant was discarded, and the white precipitate was washed thoroughly with Milli-Q water and ethanol, with three washing cycles and centrifugation after each cycle to remove residual precursors, unbound phytochemicals and other impurities. The purified ZnO NPs were dried in a vacuum drying chamber at room temperature for 24 h to obtain a white powder. The dried sample was finally stored in a desiccator.

Characterization: The optical, structural, morphological, thermal and surface properties of the synthesized ZnO NPs were examined using different analytical techniques. UV-Vis absorption spectra were recorded over 200-800 nm using a Shimadzu UV-2450 spectrophotometer to examine the optical absorption behaviour. The optical bandgap was determined from UV-Vis diffuse reflectance measurement using a Shimadzu UV-2600 spectrophotometer equipped with an integrating sphere and $BaSO_4$ reference standard. The reflectance data were converted using the Kubelka-Munk function, and the bandgap was estimated from Tauc plots. FTIR spectra were recorded in the range of 4000-400 cm^{-1} using a Shimadzu IR Prestige-2 spectrometer with KBr pellets to identify the functional groups associated with phytochemical interactions and surface stabilization. Powder X-ray diffraction (XRD) patterns were collected using a PANalytical X'Pert Pro diffractometer with Cu*K*α radiation (λ = 1.5406 Å) at 45 kV and 40 mA over a 2θ range of 10-80º. The crystalline phases and structural features were examined, and the average crystallite size was estimated using the Debye-Scherrer equation. Surface morphology and elemental composition were investigated using field-emission scanning electron microscopy (FE-SEM, JEOL JSM-7600F) equipped with an energy-dispersive X-ray spectroscopy (EDS) detector. Transmission electron microscopy (TEM, FEI Tecnai-20U Twin) and selected area electron diffraction (SAED) were used to examine particle dimensions, internal structural features and crystallinity. Thermal behaviour and the decomposition of surface associated organic constituents were studied by thermogravimetric analysis (TGA, NETZSCH STA 449 F3 Jupiter) under a N_2 atmosphere up to 750 ºC at a heating rate of 20 ºC/min. Surface area and pore characteristics were determined from

nitrogen adsorption–desorption measurements at 77 K using a BELSORB analyzer. Before analysis, the samples were degassed at 150 ºC for 6 h, and the specific surface area, total pore volume and pore size distribution were evaluated using the BET method and appropriate adsorption analysis.

***In vitro* antibacterial assay:** The antibacterial susceptibility of the biosynthesized ZnO NPs was evaluated using the agar well diffusion technique against representative Gram-negative (*Escherichia coli* ATCC 25922, *Vibrio cholerae* and *Salmonella typhi*) and Gram-positive (*Staphylococcus aureus* ATCC 25923) bacterial strains. Inocula were prepared from 18 h active cultures grown in nutrient broth at 37 ºC and turbidity-adjusted in sterile 0.85% (w/v) physiological saline to match a 0.5 McFarland standard (~1.5×10^8 CFU/mL). The adjusted bacterial suspensions were evenly spread onto sterile Mueller-Hinton Agar (MHA) plates using sterile cotton swabs. Wells of 6 mm diameter were aseptically punched into the seeded agar using a sterile cork borer. Stock suspensions of ZnO NPs were dispersed in sterile Milli-Q water *via* probe/bath ultrasonication (15 min) and loaded into designated wells at concentrations of 100, 200 and 300 µg/mL (50 µL per well). Sterile Milli-Q water (50 µL) and ciprofloxacin (10 µg/mL, 50 µL) served as the negative and positive controls, respectively. The inoculated plates were incubated under aerobic conditions at 37 ºC for 24 h. Diameters of the clear zones of inhibition (ZOI) were measured in millimeters. All assays were conducted independently in triplicate (n = 3 independent biological replicates). Data are expressed as mean ± standard deviation (SD). One-way analysis of variance (ANOVA) followed by Tukey's post-hoc test was performed to determine statistical significance between treated groups and controls ($p < 0.05$).

RESULTS AND DISCUSSION

The synthesis of ZnO NPs using an aqueous *C. medica* L. leaf extract involves interactions between zinc species and naturally occurring phytochemicals. Secondary metabolites such as polyphenols, flavonoids and carboxylic acids [17] can coordinate with zinc ions and participate in the nucleation and growth of ZnO NPs crystallites. Their adsorption onto the developing particle surfaces may regulate crystal growth and limit particle aggregation, while providing a natural stabilizing layer around the synthesized nanoparticles.

XRD studies: Powder X-ray diffraction (P-XRD) was used to determine the crystalline phase, symmetry and structural orientation of the synthesized nanoparticles (Fig. 1). The diffraction pattern exhibited distinct Bragg reflections at 2θ values of 31.82º, 33.90º, 36.40º, 47.60º, 56.70º, 62.93º and 66.55º, corresponding to the (100), (002), (101), (102), (110), (103) and (200) crystallographic planes, respectively. These reflections are characteristic of the hexagonal wurtzite structure of ZnO (JCPDS card No. 89-7102/36-1451), with a space group of $P6_3mc$, which confirm the crystalline nature of the synthesized material.

The absence of secondary reflection peaks corresponding to metallic Zn or $Zn(OH)_2$ verifies high phase purity and complete thermal conversion. The primary reflection peak at (101) indicates preferred crystal growth along this plane. The

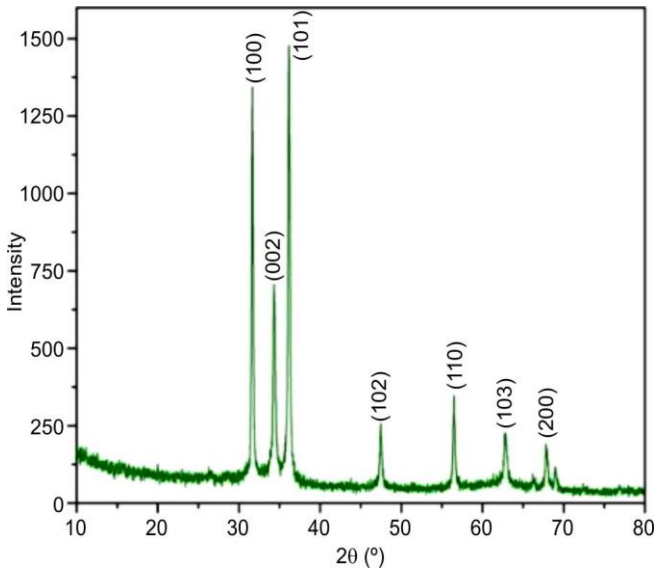


Fig. 1. Powder XRD pattern of green synthesized ZnO nanoparticles

average coherently diffracting domain size (D) was computed using the Debye-Scherrer equation applied to the primary (101) reflection (eqn. 1) [15,16]:

$$D_{101} = \frac{k\lambda}{\beta \cos\theta} \quad (1)$$

where 'k' is the shape factor (usually 0.9), 'λ' represents the wavelength of the X-ray source (Cu*K*α radiation), $\beta_{(101)}$ is the full width at half maximum (FWHM) in radians and θ is the Bragg diffraction angle. The estimated average crystallite domain size was 36.08 nm. The structural line broadening confirms the nanometer-scale dimensions of the synthesized crystallites.

Optical absorption and bandgap analysis (UV-Vis and UV-DRS): The optical response of the synthesized ZnO NPs was examined by UV-Vis absorption spectroscopy (Fig. 2a). The reaction mixture exhibited a characteristic absorption feature in the ultraviolet region, with the absorption maximum varying between 345 and 356 nm. This absorption is associated with the fundamental electronic transition in ZnO, which involve excitation from the O 2*p*-derived valence band to the conduction band. Temperature-dependent measurements revealed a distinct absorption peak at 343 nm when the reaction was carried out at 70 ºC. The well-defined absorption feature at this temperature points to a change in the optical response of the synthesized particles, potentially associated with variations in nucleation and particle growth.

To quantify the direct optical bandgap energy (E_g), UV-DRS was evaluated (Fig. 2b). The reflectance spectra were converted using the Kubelka-Munk transformation F(R):

$$F(R) = \frac{(1-R)^2}{2R} \quad (2)$$

where R is the absolute diffuse reflectance. Applying Tauc's relation for direct bandgap semiconductors:

$$[F(R)\cdot h\nu]^2 = A(h\nu - E_g) \quad (3)$$

The extrapolation of the linear portion of the Tauc plot to $[F(R)\cdot h\nu]^2 = 0$ yielded an optical bandgap of 3.32 eV (Fig.

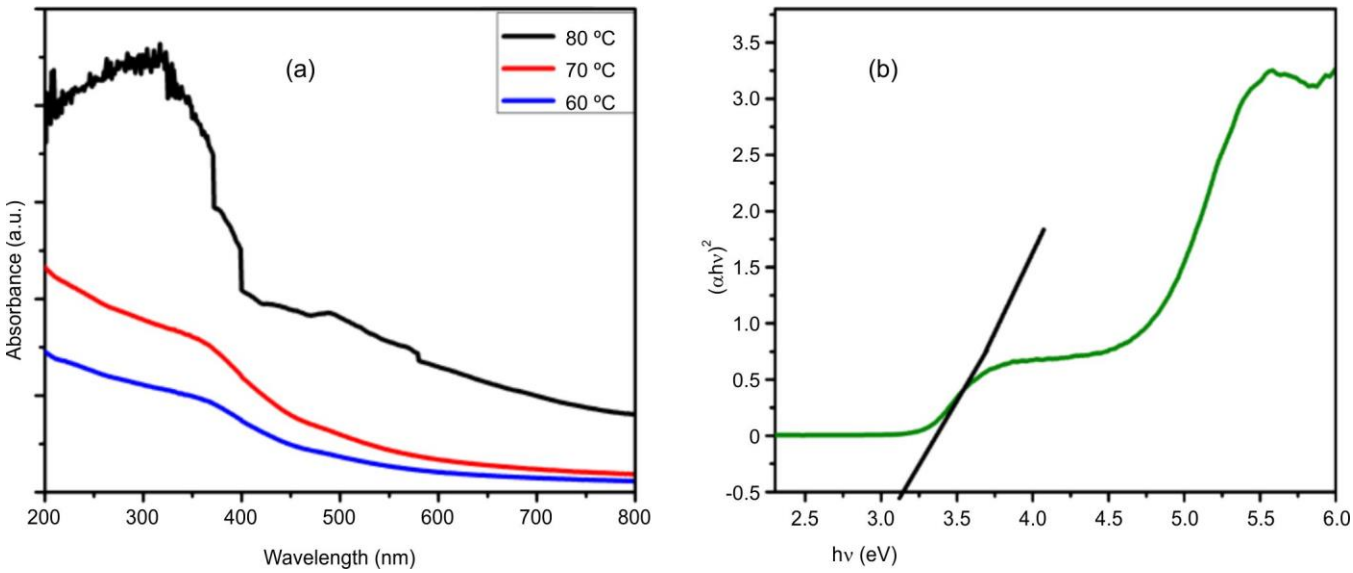


Fig. 2. UV-Vis absorption spectra of green synthesized ZnO NPs at (a) different temperatures and (b) UV-DRS spectrum

2b). Bulk single-crystalline wurtzite ZnO has a room temperature direct bandgap of approximately 3.37 eV. The measured value is therefore lower by about 0.05 eV, which represent a slight red shift in the absorption edge. The exciton Bohr radius of ZnO is approximately 2.34 nm and quantum confinement effects are generally expected when the crystallite dimensions approach a few nanometres. In the present sample, the average crystallite size estimated from XRD (36.08 nm) and the mean particle diameter obtained from TEM (59 nm) are considerably larger than this length scale. The quantum confinement is unlikely to account for the observed bandgap variation. The small difference from the bulk value may be associated with defect-related electronic states, lattice imperfections or surface interactions involving residual phytochemical species.

Infrared spectra studies: FTIR spectroscopy was employed to examine the functional groups present in the *C. medica* L. leaf extract and their association with the synthesized ZnO NPs (Fig. 3). The spectrum of the aqueous leaf extract (Fig. 3a) exhibited characteristic absorption bands at 3456 cm^{-1}, attributed to O–H stretching of phenolic and flavonoid groups; 2922 cm^{-1}, assigned to asymmetric C–H stretching of aliphatic groups; 1620 cm^{-1}, associated with carbonyl or aromatic C=C vibrations; 1411 cm^{-1} related to C–O stretching or C–H deformation and 1034 cm^{-1}, corresponding to C–O–C vibrations of oxygen-containing compounds. In the spectrum of ZnO NPs (Fig. 3b), variations in the position and intensity of these absorption bands were observed. The O–H stretching band shifted from 3456 to 3465 cm^{-1}, while the band at 1620 cm^{-1} shifted to 1640 cm^{-1}. These changes suggest interactions between oxygen-containing functional groups of the plant-derived compounds and zinc species during nanoparticle formation. A distinct absorption band at 540 cm^{-1}, accompanied by a shoulder at 562 cm^{-1}, was assigned to Zn–O lattice vibrations, further support the formation of ZnO NPs. The persistence of organic absorption bands in the nanoparticle spectrum points to the presence of plant-derived constituents associated with the particle surface.

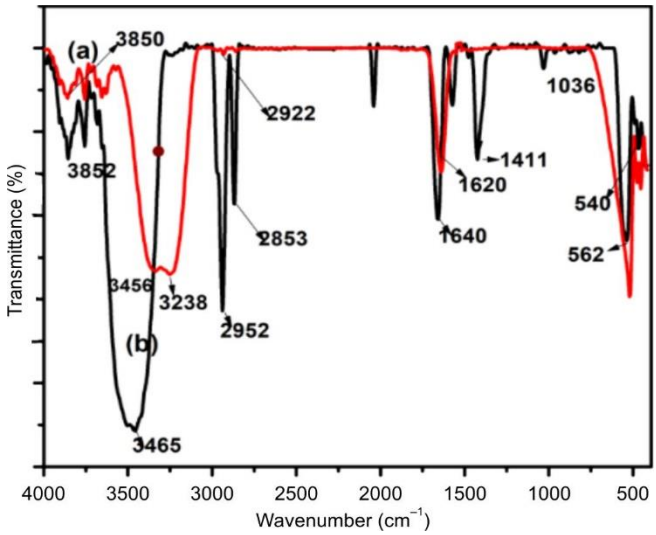


Fig. 3. FT-IR spectra of (a) aqueous leaf extract of *Citrus medica* L. and (b) ZnO NPs

Thermal studies (TGA/dTGA): The thermal stability and organic capping mass fraction of the synthesized ZnO NPs were monitored using TGA and differential thermogravimetry (dTGA) up to 730 ºC under an inert N_2 atmosphere (Fig. 4). The thermogram reveals two distinct mass-loss steps. An initial minor weight loss of approximately 2.0-2.5% occurs between 50 ºC and 150 ºC, corresponding to the evaporation of physisorbed surface moisture and residual volatile components. A major weight loss step is observed between 350 ºC and 550 ºC, corresponding to the pyrolytic decomposition of the organic phytochemical capping layer attached to the nanoparticle surfaces. The dTGA profile displays a sharp maximum mass-loss rate centered at 492.6 ºC (-0.173 mg/min), identifying the primary thermal decomposition event of the organic capping shell. Above 550 ºC the sample exhibits a nearly constant mass up to 730 ºC with a residual inorganic content of approximately 88.5 wt.% and an organic fraction of about 11.5 wt.% in the composite powder.

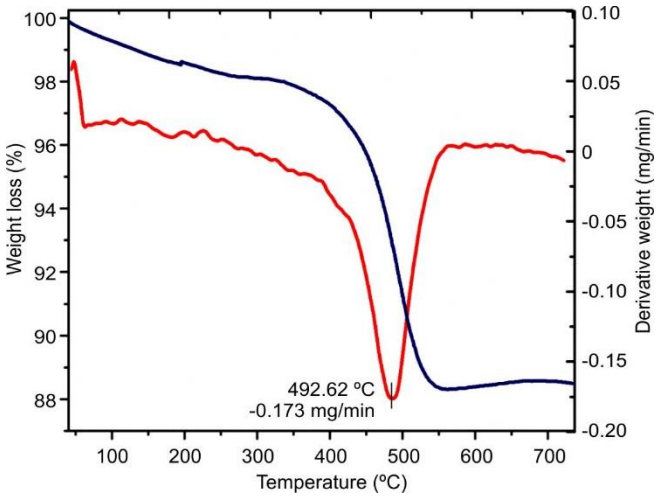


Fig. 4. TGA and dTGA of synthesized ZnO NPs using an aqueous leaf extract of *Citrus medica* L.

Surface morphology: FE-SEM micrographs (Fig. 5a-c) show the surface topography and particle distribution. The synthesized nanostructures consist of dense, uniform arrangements of quasi-spherical primary particles. Interparticle agglomeration observed at lower magnifications is driven by high surface energy and the bridging action of phytochemical capping molecules. Higher-magnification images reveal discrete primary nanograins with dimensions well below 100 nm.

Energy-dispersive X-ray spectroscopy (EDS) (Fig. 5d) confirmed the elemental composition. The spectrum displays primary peaks for Zn-L_α (1.01 keV), Zn-K_α (8.63 keV), Zn-K_β (9.57 keV) and O-K_α (0.52 keV). Quantitative microanalysis yielded an elemental composition of 76.90 wt.% Zn and 23.10 wt.% O. Within the semi-quantitative detection constraints of energy-dispersive spectroscopy, these values align reasonably with ZnO composition, with characteristic peaks for Zn and O dominating the spectrum.

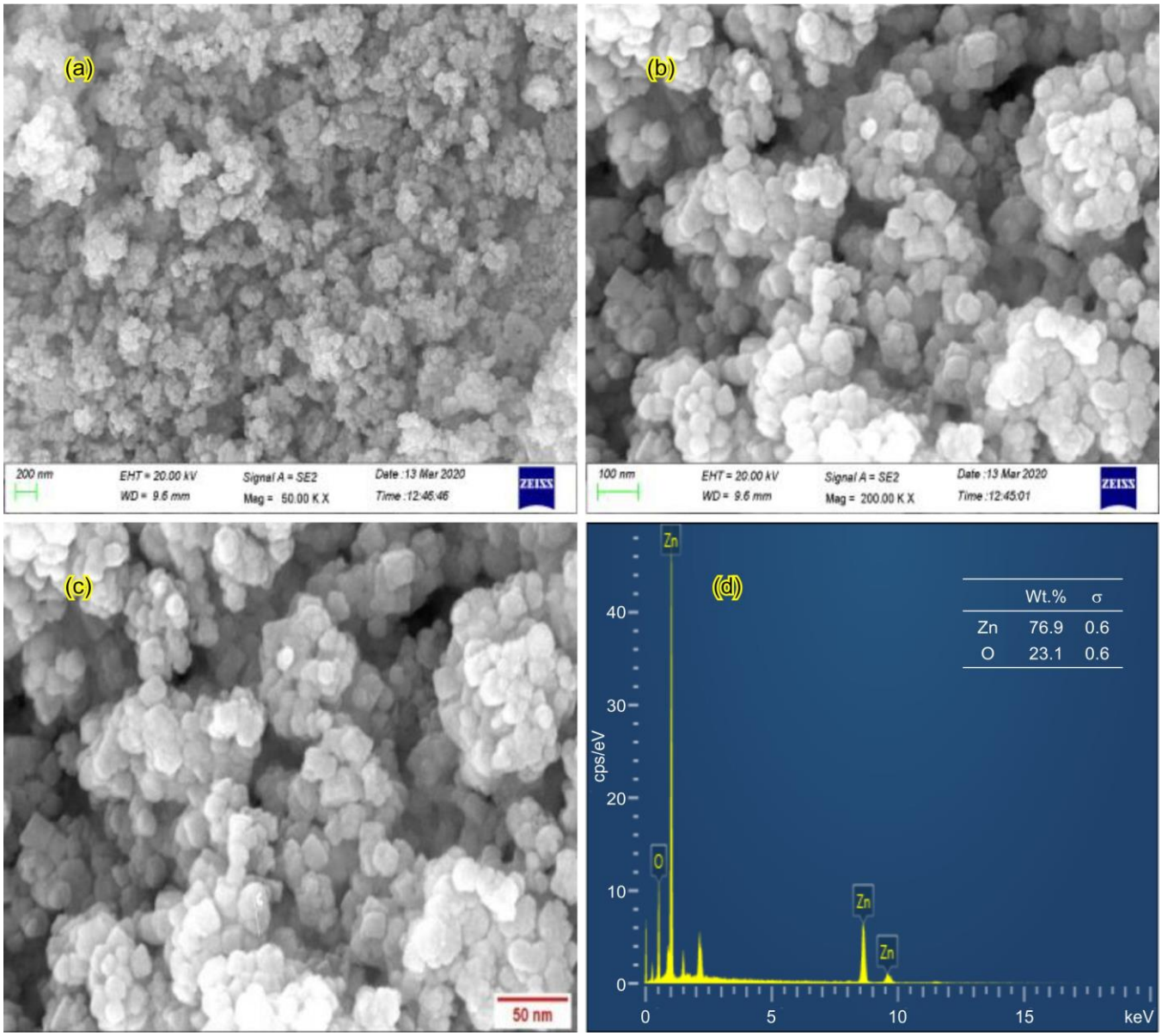


Fig. 5. (a-c) SEM images and (d) EDS spectrum of synthesized ZnO NPs using an aqueous leaf extract of *Citrus medica* L.

TEM micrographs (Fig. 6a-c) illustrate quasi-spherical nanoparticles with irregular faceted boundaries and noticeable agglomeration. Particle size measurements obtained from 100 particles in the TEM micrographs (Fig. 6d) revealed dimensions ranging from 10 to 65 nm. The size distribution was mainly concentrated between 20 and 35 nm with a reported mean particle diameter of 59 nm. The larger TEM particle diameter compared with the XRD crystallite size of 36.08 nm may arise from the presence of particles composed of multiple crystallites or the formation of small aggregates. The SAED pattern (inset of Fig. 6b) displayed distinct concentric diffraction rings indexed to the (100), (002), (101), (102) and (110) planes of hexagonal wurtzite ZnO. These diffraction features are consistent with the crystalline phase identified by powder XRD.

The SAED pattern (inset of Fig. 6b) displays distinct diffraction rings corresponding to the (100), (002), (101), (102) and (110) planes of hexagonal wurtzite ZnO. These diffraction features support the crystalline nature of the synthesized nanoparticles and are consistent with the XRD results. Nitrogen adsorption-desorption measurements at 77 K were carried out to examine the surface area and pore characteristics of the ZnO NPs (Fig. 7). The isotherm exhibited a type IV profile with an H3 hysteresis loop over a relative pressure (p/p_0) range of 0.4-1.0. This profile is characteristic of mesoporous materials with slit-shaped pores commonly formed through the aggregation of nanoparticles.

Specific surface area and pore size dynamics (BET): Quantitative Brunauer-Emmett-Teller (BET) and Barrett-Joyner-Halenda (BJH) calculations yielded a specific surface area (S_{BET}) of 35.231 m^2/g, a total pore volume (V_p) of 1.7268 cm^3/g and a mean BJH pore diameter (D_p) of 12.20 nm. This expanded surface area (35.231 m^2/g) and mesoporous pore size (12.20 nm) provide accessible active surface sites that facilitate efficient molecular diffusion and enhance reactive oxygen species generation during antibacterial and antioxidant assays.

Antimicrobial evaluation: The *in vitro* antibacterial activity of the green-synthesized ZnO NPs was screened against four bacterial pathogens using the standardized agar well diffusion assay across concentrations of 100, 200 and 300

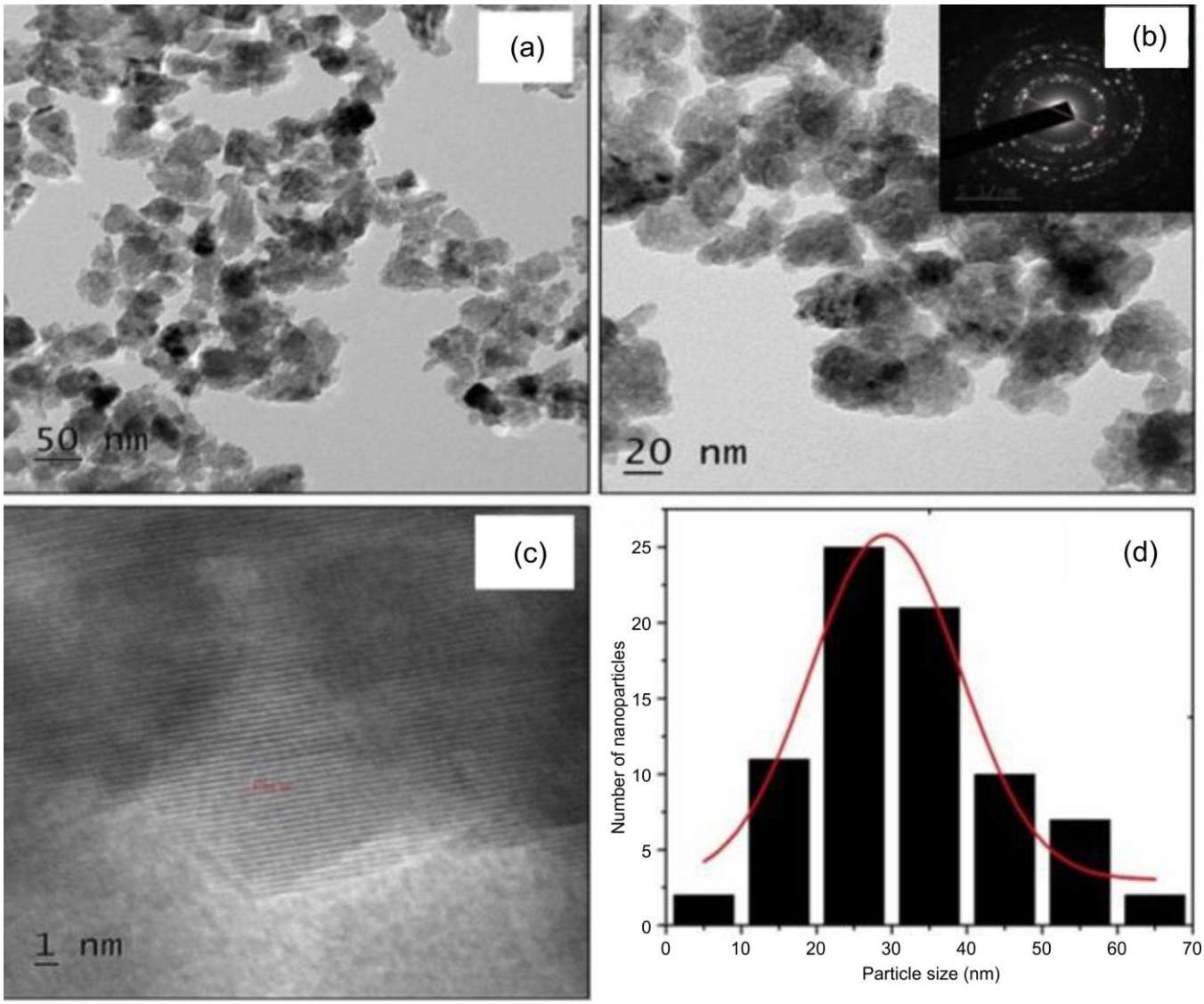


Fig. 6. (a-c) TEM images and (d) particle size distribution histograms of ZnO NPs using an aqueous leaf extract of *Citrus medica* L.

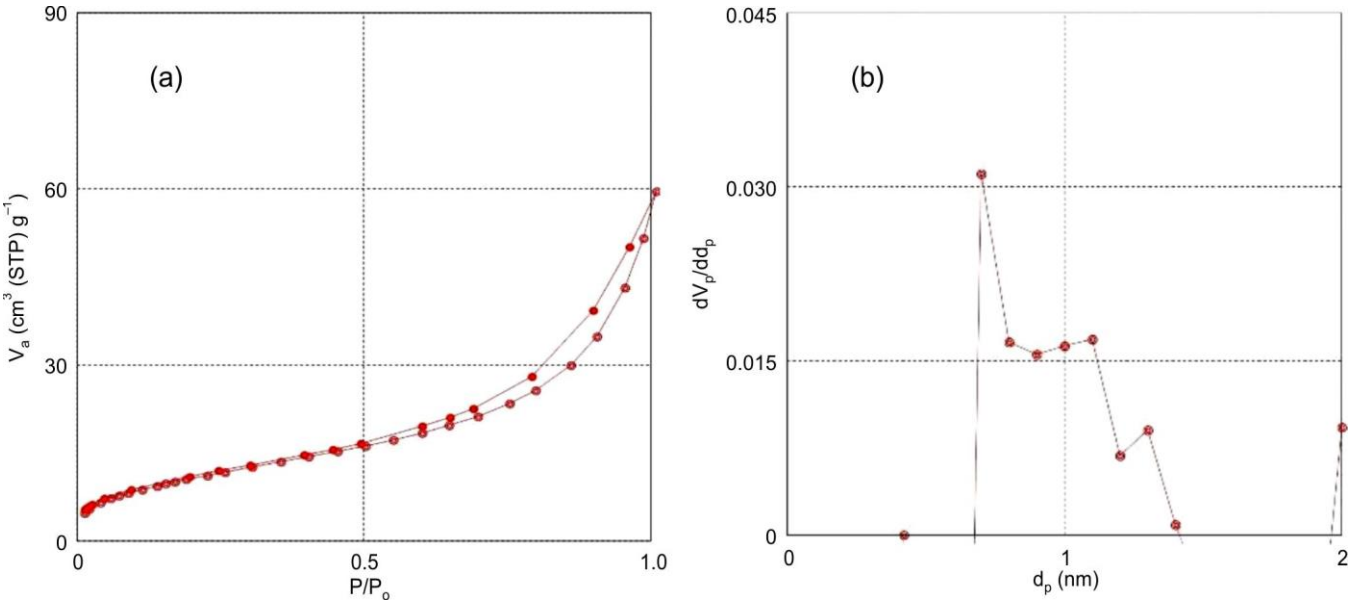


Fig. 7. (a) BET isotherm of ZnO NPs and (b) pore size distribution of ZnO nanoparticles

μg/mL (Table-1). The nanoparticles produced concentration-dependent zones of growth inhibition against all tested strains (n = 3, $p < 0.05$). Among the strains tested, Gram-negative *E. coli* showed the highest sensitivity, exhibiting an inhibition zone of 15.0 ± 0.8 mm at 100 μg/mL and reaching a maximum ZOI of 22.0 ± 1.2 mm at 300 μg/mL. In comparison, Gram-positive *S. aureus* exhibited lower sensitivity, displaying an inhibition zone of 13.0 ± 0.6 mm at 100 μg/mL and 15.0 ± 0.9 mm at 300 μg/mL. The positive control (ciprofloxacin, 10 μg/mL) produced an inhibition zone of 40.0 ± 1.5 mm, whereas the negative control (sterile Milli-Q water) showed no observable zone of inhibition.

***In vitro* antioxidant radical scavenging performance:** The radical scavenging capacity of the ZnO NPs was investigated using DPPH, H_2O_2 and reducing power assays, with butylated hydroxyanisole (BHA) as the standard reference. As shown in Tables 2 and 3, the ZnO NPs exhibited significant, concentration-dependent radical scavenging capabilities. In the DPPH assay, the radical scavenging activity of the ZnO NPs increased in a concentration-dependent manner, reaching an inhibition of 90.30 ± 1.05% at 400 μg/mL with an IC_{50} value of 90.47 ± 1.02 μg/mL. Under identical testing conditions, the commercial synthetic standard BHA exhibited an IC_{50} value of 51.56 ± 3.00 μg/mL. The antioxidant activity

TABLE-1
ZONE OF INHIBITION (mm) OF *Citrus medica* L. SYNTHESIZED ZnO NPs AGAINST PATHOGENIC BACTERIA

Pathogenic organism	Strain identifier	ZnO NPs concentration (μg/mL)			Negative control (H_2O)	Positive control (ciprofloxacin, 10 μg/mL) (mm)
		100	200	300		
Vibrio cholerae	ATCC 11623	14.0 ± 0.7	16.0 ± 0.8	19.0 ± 1.1	0 mm	40.0 ± 1.2
Staphylococcus aureus	ATCC 25923	13.0 ± 0.6	14.0 ± 0.7	15.0 ± 0.9	0 mm	40.0 ± 1.5
Escherichia coli	ATCC 25922	15.0 ± 0.8	19.0 ± 1.0	22.0 ± 1.2	0 mm	40.0 ± 1.1
Salmonella typhi	ATCC 19430	12.0 ± 0.5	14.0 ± 0.6	16.0 ± 0.8	0 mm	40.0 ± 1.4

*Well diameter = 6 mm; Sample loading volume = 50 μL. Values represent mean ZOI in mm.

TABLE-2
CONCENTRATION-DEPENDENT PERCENTAGE INHIBITION OF BHA AND ZnO NPs ON DPPH, HYDROGEN PEROXIDE RADICALS AND REDUCING POWER ASSAY

Conc. (μg/mL)	DPPH (%)		Hydrogen peroxide assay (%)		Reducing power assay (%)	
	BHA	ZnO NPs	BHA	ZnO NPs	BHA	ZnO NPs
25	34.20 ± 0.88	29.11 ± 0.75	25.23 ± 0.87	21.13 ± 0.88	33.12 ± 0.96	25.42 ± 1.33
50	51.37 ± 1.32	43.55 ± 0.98	44.12 ± 1.00	33.55 ± 0.88	48.33 ± 1.66	39.55 ± 0.87
100	65.87 ± 1.43	61.00 ± 1.45	50.44 ± 2.04	42.15 ± 2.04	62.45 ± 2.44	44.25 ± 1.88
200	77.83 ± 2.01	72.55 ± 2.03	70.24 ± 1.26	50.42 ± 1.00	75.66 ± 3.14	58.12 ± 2.66
300	86.86 ± 0.89	83.34 ± 1.33	80.96 ± 1.45	65.00 ± 0.87	84.75 ± 1.08	69.12 ± 1.88
400	96.00 ± 2.22	90.30 ± 1.05	89.61 ± 0.96	74.16 ± 0.87	92.33 ± 2.45	84.33 ± 0.99

All the values were expressed as Mean ± SEM, (n = 3). Comparisons were made between BHA *vs.* ZnO NPs; statistically significant ***$p <$ 0.001; **$p < 0.01$; *$p < 0.05$; ns = non significance.

TABLE-3
HALF-MAXIMAL INHIBITORY CONCENTRATION (IC_{50} IN μg/mL) OF STANDARD BHA AND ZnO NPs ACROSS ANTIOXIDANT ASSAYS

Sample name	50% Inhibition conc. (IC_{50})		
	DPPH radical	Hydroxyl radical	Reducing power
ZnO NPs	90.47 ± 1.02	196.56 ± 2.02	153.80 ± 1.85
BHA	51.56 ± 3.00	115.22 ± 3.00	67.29 ± 1.00

of the synthesized ZnO NPs was lower than that of the reference antioxidant BHA across all three assays. In the DPPH assay, the ZnO NPs exhibited an IC_{50} value approximately 1.75 times higher than BHA, pointing to a lower radical-scavenging capacity under the tested conditions. A similar response was observed in the H_2O_2 scavenging assay, with IC_{50} values of 196.56 ± 2.02 μg/mL for ZnO NPs and 115.22 ± 3.00 μg/mL for BHA. The reducing power assay yielded IC_{50} values of 153.80 ± 1.85 μg/mL and 67.29 ± 1.00 μg/mL for ZnO NPs and BHA, respectively (Table-3). The observed antioxidant response may partly arise from plant-derived phenolic compounds retained on the nanoparticle surfaces. Their hydroxyl groups can participate in hydrogen atom or electron donation during radical neutralization.

Conclusion

An aqueous phyto-assisted co-precipitation method was employed to synthesize zinc oxide nanoparticles (ZnO NPs) using *Citrus medica* L. leaf extract as a natural complexing and surface-stabilizing agent. Structural and optical analyses confirmed the formation of highly crystalline hexagonal wurtzite ZnO with an optical bandgap of 3.32 eV. The average crystallite size estimated from XRD was 36.08 nm while TEM analysis yielded a mean particle diameter of 59 nm with predominantly quasi-spherical morphology. FTIR and TGA analyses provided evidence of plant-derived organic constituents on the nanoparticle surfaces with an estimated organic content of ~8.5 wt.%. The material retained its inorganic structure at elevated temperatures. Nitrogen adsorption-desorption analysis revealed mesoporous characteristics with a specific surface area of 35.231 m^2/g and an average pore diameter of 12.20 nm. The ZnO NPs exhibited concentration-dependent antibacterial activity against Gram-negative (*E. coli*, *V. cholerae* and *S. typhi*) and Gram-positive (*S. aureus*) bacteria. The maximum inhibition zone was 22.0 ± 1.2 mm against E. coli at 300 μg/mL. Further investigations involving MIC/MBC determination, direct ROS detection and Zn^{2+} dissolution measurements are required to establish the mechanisms responsible for bacterial growth inhibition. The nanoparticles exhibited moderate antioxidant activity in DPPH (IC_{50} = 90.47 ± 1.02 μg/mL), H_2O_2 (IC_{50} = 196.56 ± 2.02 μg/mL) and reducing power (IC_{50} = 153.80 ± 1.85 μg/mL) assays compared with the reference antioxidant BHA. The findings establish the feasibility of using *C. medica* L. leaf extract for the aqueous synthesis of surface-functionalized ZnO NPs and provide experimental evidence of their structural, optical, antibacterial and antioxidant properties.

CONFLICT OF INTEREST

The authors declare that there is no conflicts of interest regarding the publication of this article.

DECLARATION OF AI-ASSISTED TECHNOLOGIES

During the preparation of this manuscript, the authors used an AI-assisted tool(s) to improve the language and no data, results or scientific conclusions were generated by AI. All analyses, interpretations and conclusions are the authors' own. The authors reviewed and edited the content and take full responsibility for the published work.

REFERENCES

1. N. Asif, M. Amir and T. Fatma, *Bioprocess Biosyst. Eng.*, **46**, 1377 (2023); https://doi.org/10.1007/s00449-023-02886-1
2. J. Jiang, J. Pi and J. Cai, *Bioinorg. Chem. Appl.*, **2018**, 1062562 (2018); https://doi.org/10.1155/2018/1062562
3. S. Dey, D. L. Mohanty, N. Divya, V. Bakshi, A. Mohanty, D. Rath, S. Das, A. Mondal, S. Roy and R. Sabui, *Intell. Pharm.*, **3**, 53 (2025); https://doi.org/10.1016/j.ipha.2024.08.004
4. D. Mutukwa, R. Taziwa and L.E. Khotseng, *Nanomaterials*, **12**, 3456 (2022); https://doi.org/10.3390/nano12193456
5. S. Faisal, H. Jan, S.A. Shah, S. Shah, A. Khan, M.T. Akbar, M. Rizwan, F. Jan, Wajidullah, N. Akhtar, A. Khattak and S. Syed, *ACS Omega*, **6**, 9709 (2021); https://doi.org/10.1021/acsomega.1c00310
6. T.U. Doan Thi, T.T. Nguyen, Y.D. Thi, K.H. Ta Thi, B.T. Phan and K.N. Pham, *RSC Adv.*, **10**, 23899 (2020); https://doi.org/10.1039/D0RA04926C
7. A. Molla, M.M. Hoque, F.T. Richi, M.H. Kabir, S. Alam, N.U. Ahmed, N.U. Emon, C. Shao, C. Zeng, S. Wang, P. Geng and A.A. Mamun, *Int. J. Nanomedicine*, **20**, 4803 (2025); https://doi.org/10.2147/IJN.S493905
8. S.U.R. Qamar and J.N. Ahmad, *J. Mol. Liq.*, **334**, 116040 (2021); https://doi.org/10.1016/j.molliq.2021.116040
9. J. Singh, T. Dutta, K.-H. Kim, M. Rawat, P. Samddar and P. Kumar, *J. Nanobiotechnology*, **16**, 84 (2018); https://doi.org/10.1186/s12951-018-0408-4
10. S. Ahmed, M. Ahmad, B.L. Swami and S. Ikram, *J. Adv. Res.*, **7**, 17 (2016); https://doi.org/10.1016/j.jare.2015.02.007
11. S.S. Salem and A. Fouda, *Biol. Trace Elem. Res.*, **199**, 344 (2021); https://doi.org/10.1007/s12011-020-02138-3
12. H. Agarwal, S. Venkat Kumar and S. Rajeshkumar, *Res.-Effic. Technol.*, **3**, 406 (2017); https://doi.org/10.1016/j.reffit.2017.03.002
13. S.S. Elhady, A.S. Wahba, A.K. Ibrahim, G.S. El-Sayyad, A.I. El-Batal, N.S. Wahba, M.S. Nafie, S.A. Ahmed, A.K. Ibrahim, J.M. Badr, S.S.A. Murshid, A.A. Bagalagel, E.S. Habib and R.F.A. Abdelhameed, *ACS Omega*, **10**, 36178 (2025); https://doi.org/10.1021/acsomega.5c03992
14. Y.R. Lamichhane, K. Parajuli and S.S. Pradhanang, *Sci. World*, **17**, 99 (2024); https://doi.org/10.3126/sw.v17i17.66441
15. P.M. Kibasomba, S. Dhlamini, M. Maaza, C.-P. Liu, M.M. Rashad, D.A. Rayan and B.W. Mwakikunga, *Results Phys.*, **9**, 628 (2018); https://doi.org/10.1016/j.rinp.2018.03.008
16. F.T.L. Muniz, M.A.R. Miranda, C.M. Dos Santos and J.M. Sasaki, *Acta Crystallogr. A Found. Adv.*, **72**, 385 (2016); https://doi.org/10.1107/S205327331600365X
17. E. Santhiya, M. Jasline Pravina, A. Vengadeswari, S.M. Ramalekshmi, D.C. Anushiya, R. Uma, R. Mahesh, B. Parthipan, *Mukt Shabd J.*, **11**, 701 (2022).